2022

Relative Radiometric Correction of Pushbroom Satellites Using the Yaw Maneuver

Christopher Begeman
South Dakota State University, christopher.begeman@jacks.sdstate.edu

RELATIVE RADIOMETRIC CORRECTION OF PUSHBROOM SATELLITES USING THE YAW MANEUVER

BY

CHRISTOPHER BEGEMAN

A thesis submitted in partial fulfillment of the requirement for the

Master of Science

Major in Electrical Engineering

South Dakota State University

2022

THESIS ACCEPTANCE PAGE

Christopher Begeman

This thesis is approved as a creditable and independent investigation by a candidate for the master's degree and is acceptable for meeting the thesis requirements for this degree. Acceptance of this does not imply that the conclusions reached by the candidate are necessarily the conclusions of the major department.

Dennis Helder
Advisor Date

George Hamer
Department Head Date

Nicole Lounsbery, PhD
Director, Graduate School Date

ACKNOWLEDGEMENTS

First, I would like to thank my advisors Dr. Helder and Larry Leigh for making this opportunity possible in the troubling COVID times. I truly appreciate all they have done for me in terms of guidance, patience, and support while in pursuit of my Master's degree. Without them none of this would be possible.

I would also like to thank the image processing laboratory members Dr. Cibele Teixeira Pinto, Mrs. Morakot Kaewmanee, and all my classmates for making the lab feel like a home away from home.

Finally, I would like to thank my father, mother, two sisters, and grandparents for their love and support in the most challenging of times.

CONTENTS

ABSTRACT

RELATIVE RADIOMETRIC CORRECTION OF PUSHBROOM SATELLITES USING THE YAW MANEUVER.

CHRISTOPHER BEGEMAN

2022

Earth imaging satellites commonly acquire multispectral imagery using linear array detectors formatted as a pushbroom scanner. Landsat 8, a well-known example, uses pushbroom scanning and thus has 73,000 individual detectors. These 73,000 detectors are split among 14 different focal plane modules (FPM), and each detector and FPM exhibit unique behavior when monitoring a uniform radiance value. To correct for each detectors differences in sensor measurement a novel technique of relative gain estimation that employs an optimized modified Signal-to-Noise Ratio through a 90˚ yaw maneuver, also known as side slither, is presented that allows for both FPM and detector level relative gain calculation. A periodic model based on in-scene FPM corrections was designed as a go-to model for all bands aboard Landsat 8. Relative gains derived from the side slither technique and applied to imagery provide a visual and statistical reduction of detector level and FPM level striping and banding in Landsat 8 imagery. Both reflective and thermal wavelengths are corrected to a level that rivals current operational methods. While Landsat 8 is used as an example, the methodology is applicable to all linear array sensors that can perform a 90˚ yaw maneuver.

1. INTRODUCTION

1.1. Radiometric Calibration

Multispectral Earth data, i.e. electromagnetic radiation, is acquired through the use of imaging sensors onboard earth imaging satellites. Normally, Earth imaging sensors, after detection, amplification, and analog-to-digital conversion, convert the level of electromagnetic radiation at the aperture into a digital number (DN) that has no units. Radiometric calibration is the process of converting DN values into physical units, such as reflectance, for analysis. However, the multi spectral data acquired by the sensors tend to be influenced by multiple factors leading to non-uniformities including atmospheric scattering and absorption, differences in sensor manufacturing, electrical noise, and differences in each detector's gains and linear responses, which will change over time. With recently launched satellites having more spectral bands than their previous counterparts, and therefore many more detectors to calibrate, a useful and efficient calibration method is needed to remove the non-uniformities across detectors in each spectral band. This paper illustrates the efficacy of using the yaw maneuver, also known as the side slither (SS) technique, as defined in Section 3.1, to derive relative gains between detectors and across an entire detector array. The organization of this paper is as follows: Introduction, Background, Methodology, followed by Results \& Discussion, and ending with the Conclusion.

1.1.1. Relative Gain Corrections

Due to detectors portraying non-uniformities when measuring the same level of incident light an artifact called streaking tends to appear in non-calibrated earth satellite

images. The difference between detectors measuring the same level of incident light is called detector level streaking. To correct for this detector level streaking, a detector relative gain is needed. Detector relative gains can be acquired in a multitude of ways, some easier than others. However, these corrections are only useful within their respective focal plane modules (FPMs). To correct between FPMs a different relative gain value is needed called the FPM relative gain.

Focal plane modules are separately constructed arrays of detectors that tend to have differing amounts of offset between each module. These offsets are due to similar reasons that the detectors have non-uniformities and are mitigated in a similar fashion. As an example, Figure 1, a Landsat 8 image and our sensor of reference for this study, shows both detector level streaking as well as FPM differences that need correction.

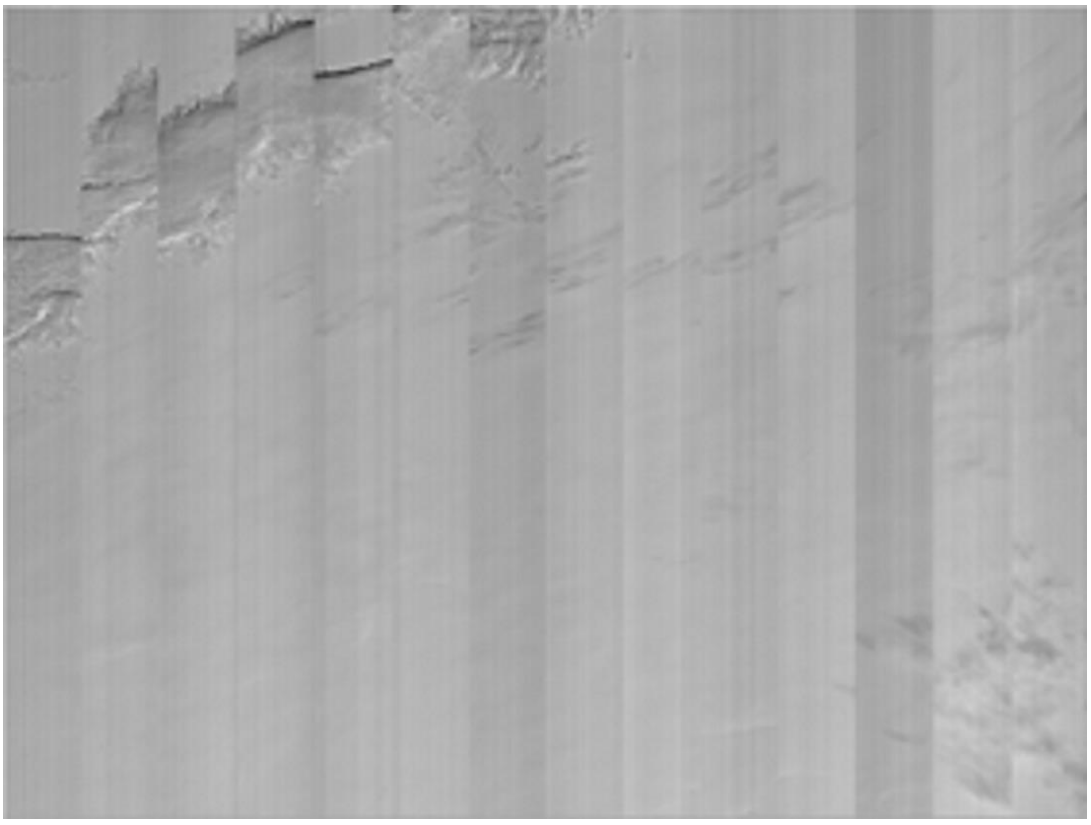

Figure 1. Green band test image of Greenland. The thick vertical discolorations are FPM level streaking and contained within them are thin vertical stripes which are detector level streaking.

1.2. Landsat 8

Landsat 8 is one of two operational Landsat satellites whose goal is to provide moderate resolution measurements of Earth's surface in the visible, near infrared (NIR), shortwave infrared (SWIR), and thermal infrared (TIR) wavelengths. Landsat 8 is composed of two different imaging systems: the Operational Land Imager (OLI) for shorter wavelengths, and the Thermal Infrared Sensor (TIRS) for longer wavelengths. Both OLI and TIRS utilize pushbroom scanning to acquire imagery as opposed to whiskbroom scanning used by all other previous Landsat satellites. OLI was designed, built, and tested by Ball Aerospace and Technology Corp., while NASA Goddard Space Flight Center did the same for TIRS. Landsat 8 images span the entire globe and each image comes in a

path/row format where each path is one sweep north to south around the earth. A detailed description of the Landsat world reference system (WRS) can be found on the NASA website [1].

1.2.1. Scanner Types

Primarily, there are two different scanner types used by the Landsat family for remote sensing from space. The first, and older, of the scanning types is that of a whiskbroom scanner. A whiskbroom scanner uses a scan mirror assembly to produce a cross-track scanning motion to reflect light onto one detector. The cross-track scanning motion resembles that of a whiskbroom and is useful when the satellite is limited on the number of detectors available. To provide the across-track motion needed by the whiskbroom scanners, a mechanical motion is needed. The across track motion is created by a pair of moving mirrors called the scan line corrector and can be prone to mechanical failure as shown by the scan line correction mirror failure that occurred on the Landsat 7 satellite [2].

Pushbroom scanning is the second of the scanning types used by the Landsat family. A pushbroom scanning motion uses an array of detectors perpendicular to the flight path of the satellite resulting in a motion that resembles that of pushbroom. Due to the pushbroom scanning method many more detectors are needed to create an image and each detector will inevitably have a unique sensitivity as compared to its neighbors [3]. To correct for these varying sensitivities, an overarching calibration method is needed to

simultaneously radiometrically correct each detector individually. Figure 2 shows a comparison between scanning types.

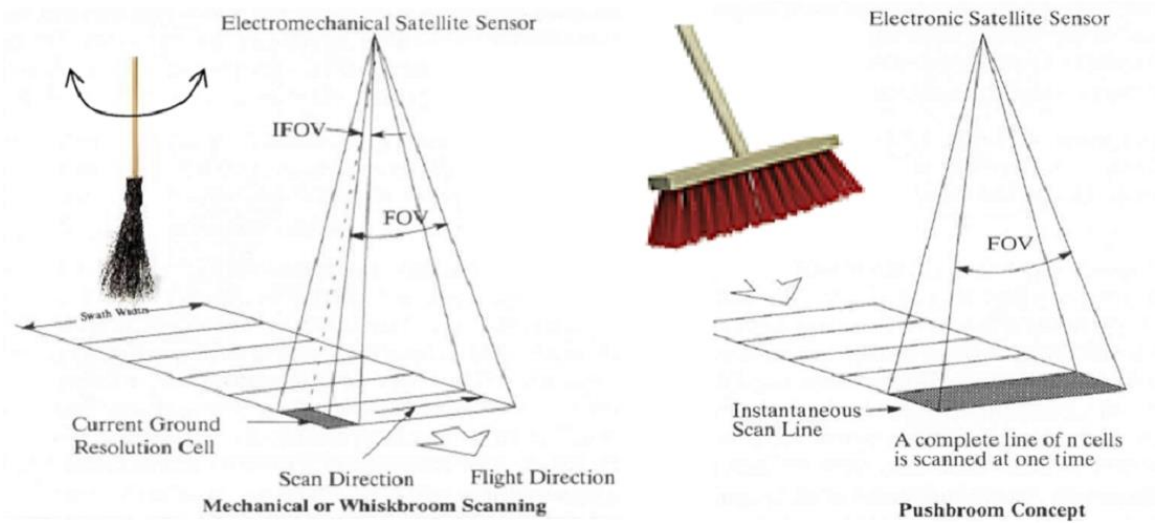

Figure 2. Whiskbroom (left) vs Pushbroom (right) Scanning Methods [4].

1.2.2. OLI

The Operational Land Imager (OLI) is used to image a wide array of spectral wavelengths from the visible out to the shortwave infrared. The full spectral coverage and resolution of the OLI sensor can be found in Table 1.

Table 1. OLI Spectral Bands and Resolution [3].

Band Number	Band Name	Bandwidth (nm)	Resolution (m)	Detector Count (per FPM)
1	Coastal/Aerosol	435 – 451	30	494
2	Blue	452 – 512	30	494
3	Green	533 – 590	30	494
4	Red	636 – 673	30	494
5	NIR	851 – 879	30	494
6	SWIR – 1	1566 – 1651	30	494
7	SWIR – 2	2107 – 2294	30	494
8	Panchromatic	503 – 676	15	988
9	Cirrus	1363 – 1384	30	494

Within OLI are 14 different detector arrays, or FPMs, each containing 494 detectors, except for Band 8, which has 988 detectors, per module. Each FPM within OLI is staggered causing an even/odd pattern, and within each FPM, each detector is staggered in an even/odd fashion, as shown in Figure 3.

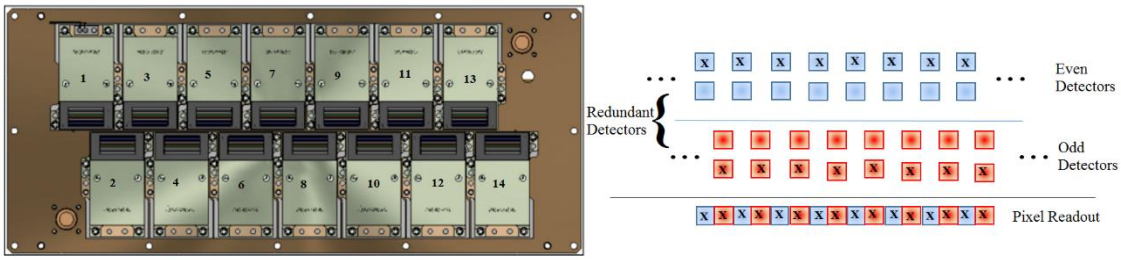

Figure 3. FPM level staggering (left) and Detector level staggering (right) [5].

OLI also contains two different sets of detector types to measure different wavelengths. Bands 1-5 and 8 consist of silicon p-intrinsic-n detectors (SiPIN) to measure visible to near infrared wavelengths, while bands 6, 7, and 9 consist of mercury-cadmium-telluride (HgCdTe) detectors to measure shortwave infrared wavelengths [3].

1.2.3. TIRS

The Thermal Infrared Sensor (TIRS) is used to create thermal images of the Earth's surface with a lower spatial resolution than that of OLI and consists of bands designated as 10 and 11. The spectral range and resolution of TIRS can be found in Table 2.

Table 2. TIRS Spectral Bands and Resolution [3].

Band Number	Band Name	Bandwidth (nm)	Resolution (m)	Detector Count (per FPM)
10	TIRS – 1	10600 – 11190	100	640
11	TIRS - 2	11500 – 12510	100	640

Unlike OLI, TIRS only has three FPM's, also known as sensor chip assemblies (SCA), consisting of 640 detectors each. Like OLI, these FPM's are staggered in an even/odd pattern, as are the detectors within the FPM, as shown in Figure 4. TIRS consists of quantum well infrared photodetectors (QWIPS) to detect thermal wavelengths of light that are related to Earth's surface temperature.

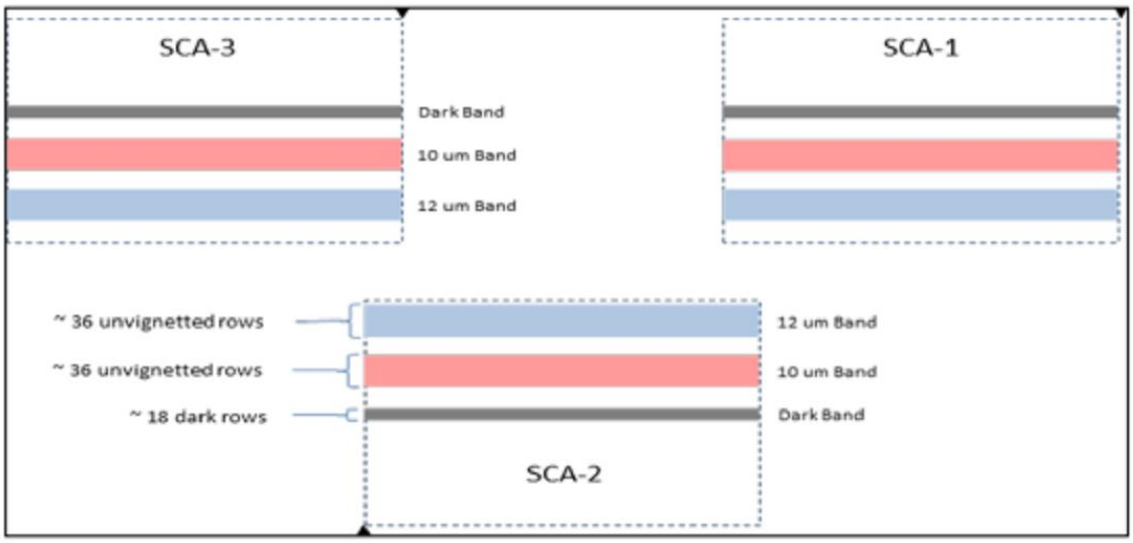

Figure 4. TIRS FPM level offsets [3].

2. BACKGROUND

2.1. Current Methods for Relative Gain Estimation

Currently, there are multiple methods for relative gain estimation. To estimate relative gains, statistical information obtained from the data collected from each detector can be used to estimate detector relative gains. Said statistical information can be obtained in multiple ways including: the imaging of a bright uniform target, the tracking of a detector's average value over time, and comparing the detectors measurement to a known or modeled value.

2.1.1. Solar Diffuser Panel

There are multiple ways to remotely calibrate detectors using uniform bright light. Knight and Kvaran (2014) explore a method where a solar diffuser panel is used to illuminate all detectors within Landsat 8 [6]. This is the current method used by Landsat 8 where a solar diffuser panel deployed in front of the aperture of the OLI reflects light from

the sun and scatters the intensity evenly across the array of detectors so that each detector views the same high intensity amount of light. With an ideal diffuser panel and ideal detectors, the diffuser panel image would be a uniform image; however, there are detector level differences across the diffuser image. It is these differences that are the basis behind the relative gain calculations. Unfortunately, this method tends to vary over time as the solar diffuser panel acquires impurities that affect accuracy of the calibration. Specifically, detectors located within the end FPMs, FPM 1 and 14 for OLI bands, tend to receive less light than those in the middle creating negative impacts on the relative FPM and detector gains.

2.1.2. On-Board Lamp

High intensity light can be artificially created using multiple on-board lamps. This method uses a lamp that creates a bright light that is nearly uniform at all wavelengths to provide an invariable target for the detector arrays to measure. From these measurements, each detector can be calibrated across an array and then across each FPM as each detector should ideally be measuring the same value. Unfortunately, this method decays the more the on-board lamp is used resulting in a decrease of radiance being emitted by the lamp. The decrease in output from the lamp creates a change in the relative gain values and therefore negatively affects the overall calibration of the instrument [7].

2.1.3. Lifetime Statistics

Lifetime statistics provide a method to calculate relative gains for detectors without needing extra on-board calibrators or imaging motions. Shrestha (2010) demonstrates a

method of calculating relative gains using all available uncalibrated images. From the uncalibrated images the number of pixels were calculated and the mean and standard deviation from each detector was recorded to find an average difference between detectors. The authors show that the streaking within an image is reduced, when compared to uncalibrated images, due to their relative gain calculations [8]. The drawbacks of this method include the need to have a large image set to produce a quality relative gain estimate, as well as the need to process large amounts of data.

2.1.4. Histogram Statistics

The 'Histogram statistics' method is another form of relative gain estimate in which on-board calibrators and imaging maneuvers are not needed. Wegener (1990) show a method in which the probability density function for each detector is calculated and stored in a look up table. Then, based on the radiance of the pixel and the detector used in an image a new radiance value is found. To calculate the probability density function uniform sub image regions were chosen where each detector produced at least one value in the image and then histograms were taken of the sub image regions based on each detector. The histograms were then aligned between detectors to determine the relative gain values needed for the probability density functions [9]. In a whiskbroom scanner this method works well as fewer detectors are needed to produce an image. However, in a pushbroom scanner where there are thousands of detectors this would be an unviable method of calibration without using entirely uniform images. Another drawback of this method is that images with a uniform region are needed to calculate the relative gain values.

2.1.5. Side Slither

Side slither is a relatively new calibration method that came about due to the use of pushbroom scanners as opposed to whiskbroom scanners. The side slither was first performed by Cook, et al. in 2001 and the technique has been improved on since [10]. A side slither maneuver, also known as a yaw maneuver, which will be discussed later in greater detail, requires a special yaw rotation by the satellite in which the detector arrays move from being in a cross-track direction to an along-track direction. Bright uniform regions of the earth are imaged while using the side slither maneuver to acquire a long data collect where each detector ideally measures the same uniform value; however, due to the non-uniformities in each detector and detector array, each detector measures a slightly different value. It is the measurement differences that allow for the side slither method to calculate relative gains to remove streaking in images. Pesta, et al. (2015) was the most recent study to portray the usefulness of side slither, and determined that the most ideal places for side slithers to take place were over Greenland, Antarctica, and North Africa [11]. Specific locations for the Landsat 8 satellite for each of the side slithers can be found in Table 3.

Table 3. Summary of Side Slither path/row location acquisition

Location	Path	Row
Greenland	4	5-21
Antarctica	88	107-117
North Africa	187	41-46

The advantages of using side slither will be discussed in the following section and the limitations in the method are explored. Landsat 8 is the earth imaging satellite used for

this study; however, it should be noted that many earth imaging satellites stand to benefit from this in-depth work of best usages, when implementing side slither methodologies.

3. METHODOLOGY

Estimating relative gains using the side slither method is carried out in two major steps. The first of these steps is performing the satellite yaw rotation. The second of these steps is correcting the data using computer algorithms. Here, the steps and reasoning behind each action taken will be provided.

3.1. Side Slither Maneuver

Side slither data is acquired through a simple yaw rotation of the pushbroom satellite. The line-by-line imaging of pushbroom scanners are utilized in the yaw maneuver where the pushbroom scanner is rotated ±90° in the yaw direction and whole lines of data can be collected where each detector should ideally scan the same spot on the earth. The direction of yaw rotation is Landsat 8 \& 9 specific, and depends on the location of the side slither collect. Collects in the northern hemisphere will be rotated +90°, and locations in the southern hemisphere will be rotated -90°. The change in rotation is done to avoid direct sunlight exposure at the solar port when the satellite images at the top or bottom of its orbit. The ideal side slither locations are highly reflective uniform areas, such as snow or sand covered locations, to minimize the non-idealities that may occur from variations in ground cover.

3.2. Data Processing for Landsat 8 OLI

This section describes the algorithmic processing of data specifically for Landsat 8. Full descriptions of the processes can be found in the Algorithm Description Document (ADD) of Landsat 8 [12]. Figure 5 contains the OLI processing flow used here and is a summarized version of the OLI radiometric processing overview contained in the ADD. The TIRS processing flow is nearly the same as the OLI processing with a few key step differences as explained in further detail.

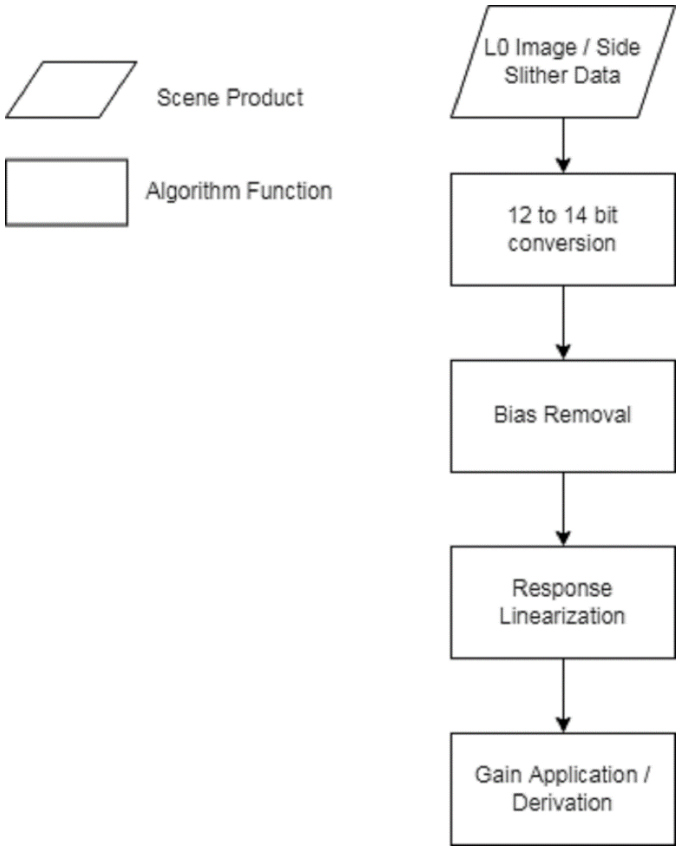

Figure 5. Summarized OLI radiometric processing overview used to prepare side slither data for relative gain extraction and Level 0 or raw images for relative gain application

The data being processed in the following descriptions is the side slither data collected by Landsat 8 and requires the same processing regardless of side slither location.

Each side slither data collection was acquired with the help of USGS EROS. Data is processed for each FPM individually starting with FPM 1.

3.2.1. 12-to-14 bit Conversion

With the OLI sensor onboard Landsat, all data down-linked from OLI is in 12-bit resolution; however, the OLI sensor itself is a 14-bit sensor. Because of conversion of the analog signal to a digital format in the sensor, quantization noise occurs. Quantization noise comes into effect when an image has too few quantization levels, i.e. bit levels, and with the last two bits of the sensor being empty, Gaussian noise needs to be reintroduced. To return the resolution of the data back into a 14-bit format the data were multiplied by a factor of 4 and the Gaussian noise was restored using equation 1

$$DN_{14}(b,d) = (DN_{12}(b,d) * 4) + \omega \quad (1)$$

where DN_{12} is the 12 bit level-0 data that was read in, ω is white Gaussian noise with values between 0 and 1, b is per band, and d is per detector. As TIRS is a 12-bit sensor and does not need the correction, this step was omitted when processing data from the TIRS sensors.

3.2.2. Bias Subtraction

With the OLI sensor onboard Landsat, all data down-linked from OLI is in 12-bit resolution; however, the OLI sensor itself is a 14-bit sensor. Because of conversion of the analog signal to a digital format in the sensor, quantization noise occurs. Quantization noise comes into effect when an image has too few quantization levels, i.e. bit levels, and with the last two bits of the sensor being empty, Gaussian noise needs to be reintroduced. To return the resolution of the data back into a 14-bit format the data were multiplied by a factor of 4 and the Gaussian noise was restored using equation 2

$$DN_b(b,d) = DN_{14}(b,d) - B(b,d) \quad (2)$$

where DN_{14} is the calculated 14 bit DN values, B is the bias value per band per detector read in from the calibration parameter file (CPF), and DN_b is the bias subtracted DN. Bias values for Landsat 8 are located in the CPF which can be downloaded from the USGS website [13].

3.2.3. Linearize Image

Unfortunately, each detector does not respond linearly to incident light and, therefore, needs to be linearized based upon the intensity. The linearization process consists of a per detector quadratic equation based upon the intensity of incident light with three different equations for low, medium, and high intensity light as shown in equation 3

$$DN_L = p[0,s] + p[1,s] * DN_b + p[2,s] * DN_b^2 \quad (3)$$

where DN_L is the linearized DN values, p is the quadratic parameter based on signal level s and parameter number 0-2, and DN_b is the bias subtracted DN value. The linearization parameters can be found in the response linearization look up table (RLUT) files located on the USGS website [14].

Due to TIRS detectors being slightly more nonlinear when compared to OLI detectors, a second linearization sttep is needed. While the first linearization step as explained above is to be applied to TIRS data before being bias subtracted, the second linearization step for TIRS is similar to the OLI linearization in that it occurs after bias subtraction, however, the calculation is slightly more complicated. A full step by step instruction of the TIRS second linearization process can be found in the Landsat 8 ADD [12].

3.3. Pushbroom Satellite Relative Gain Algorithm

The following section is dedicated to the portion of the relative gain algorithm that is not specifically designed for Landsat 8 and can be applied to most pushbroom scanning satellite. Exceptions include those that do not have separated focal plane modules.

3.3.1 Pixel Shift

In normal imaging mode of Landsat 8, the 7000+ detectors aboard OLI and TIRS are oriented in a cross-track direction orthogonal to the velocity vector of the satellite. However, in side slither mode the detector arrays are oriented ±90 degrees in the yaw direction, to enable each detector to measure the same spot on earth, and ideally output the same DN value. Due to how surface imaging satellites orbit the earth, a shift will occur in the data collected by each detector. Figure 6 shows a simplified version that ignores some of the complexities of acquisition (i.e. Earth rotation, atmospheric path, and altitude of data collected) of the shift in data that occurs.

To correct for this shift in data, a circular shift algorithm was used to shift detector level data forwards or backwards by the detector number minus one, i.e. the second detector would be shifted one pixel forward or backward while the 494th detectors data would be shifted 493 pixels backwards or forwards. The direction of shift was dependent upon the direction of yaw rotation as the side slither occurred; forward shift for northern hemisphere collects and negative shift for southern hemisphere collects. The shift needed depends on

location of the side slither as the orientation of the maneuver differs between northern and southern latitudes due to the difference in positive and negative yaw rotation.

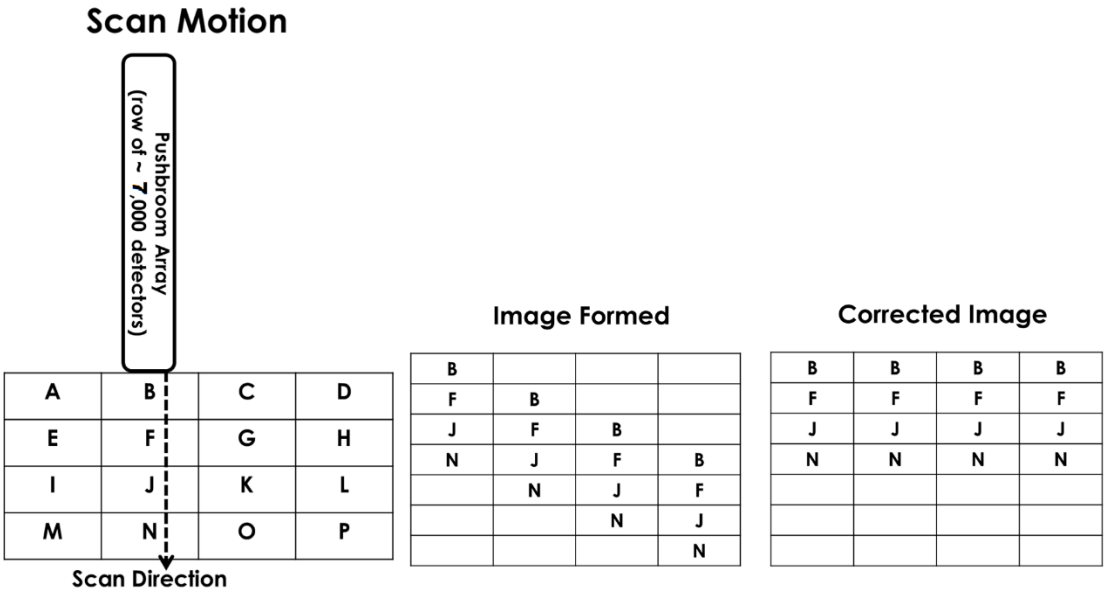

Figure 6. Side Slither being performed (left); Shifted image formed from scan line error (middle); Pixel Shifted image (right).

3.3.2. Uniform Frame Selection

After the side slither data were pixel shifted, a uniform region needed to be selected to derive the most ideal detector relative gains. To find the most uniform region within a side slither, the detector Signal-to-Noise ratio (SNR) was used. Snow and desert covered areas were chosen as the ideal locations for side slithers to occur as these two land cover types collectively have high signal and high uniformity for all wavelengths within OLI and TIRS. Acquiring high signal data during the side slither maneuver is important to prevent noise from having a major effect on detector relative gain estimates because the noise within a detector does not nominally increase at a greater rate than linearly when compared

to signal, so a rise in signal strength reduces the overall effect of noise within the data. Figure 7 shows the spectral reflectance of snow and sand as well as the bands of Landsat 8 to show that a relatively high signal can be achieved at all wavelengths. For the visible to near infrared (VNIR) bands, i.e. bands 1-5 & 8, snow scenes provide a high SNR value, and sand scenes in North Africa provide the best SNR for the shortwave infrared (SWIR) bands, i.e. bands 6 and 7, when compared to other land cover types.

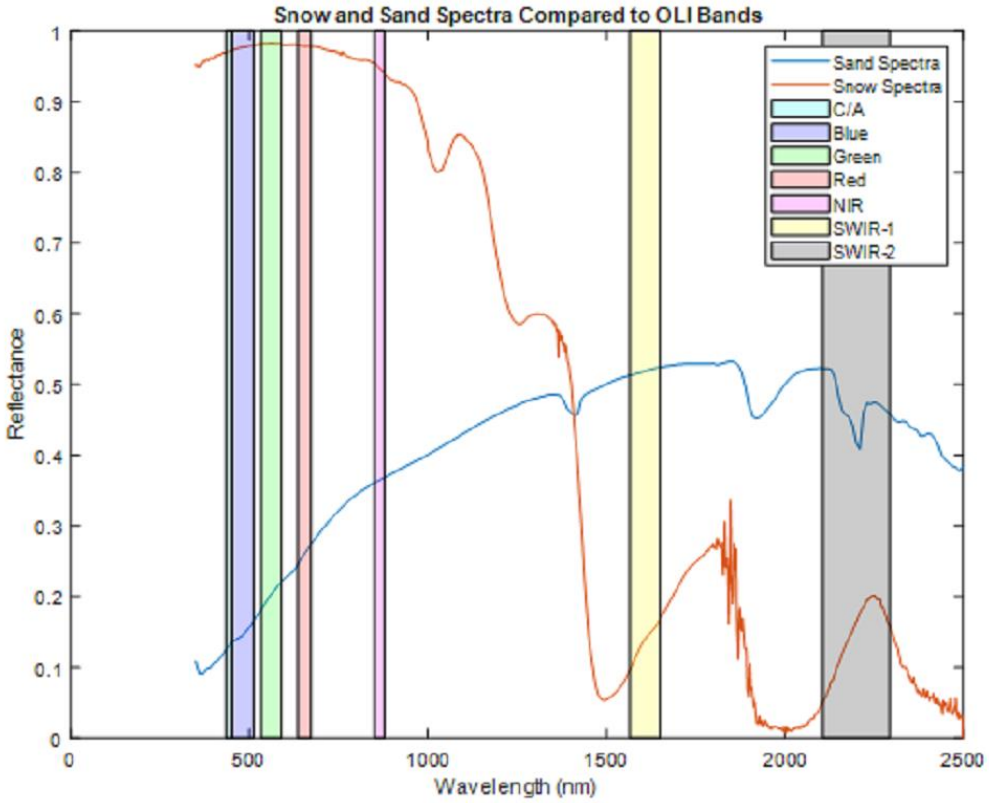

Figure 7. Snow and Sand Spectra over OLI bands showing snow having a high signal value for VNIR bands and sand having a high signal value for SWIR bands [15] [16].

SNR calculations are normally the signal divided by the noise where noise is expressed as the standard deviation of the data since we are assuming the signal is constant in homogeneous image regions. However, some areas within the side slither paths contain

non-uniform high signal regions. To avoid high signal areas that are noisy in a side slither, and capture the most uniform regions, the noise was given a greater weight in the SNR calculation by using variance as opposed standard deviation as shown in equation 4

$$SNR_i' = \overline{DN}_{Li}/Var_i \quad (4)$$

where SNR' is the modified signal-to-noise ratio across i frames where a frame is the same temporal instance of measurement for all 498 detectors within an FPM, DN_{Li} is the average linearized DN value across all detectors throughout i frames, and Var is the variance of all detectors across i frames. The SNR' was then calculated for each frame of the side slither data and the region with the highest SNR' was chosen. The more uniform frames that were used, the lower the instrument noise, as instrument noise has a Gaussian distribution and is averaged to zero at large amounts of frames. The minimum number of frames selected that provided satisfactory relative gains was at least 5% of the side slither length. With 5% as the minimum number of frames, the number of frames was expanded to include all consecutive uniform frames within the side slither to reduce the instrument noise as much as possible. To accomplish this frame selection expansion, the number of frames chosen was increased in 5% increments with the first step being from 5% of the total frames available to 10% of the total frames available for SNR' comparison. The SNR' of the frames chosen from 10% of the SS was compared to the SNR' of the frames chosen from 5% of the SS, and if the SNR' did not decrease by more than 10%, then the larger number of frames was chosen. This 5% iterative frame expansion process was completed until the calculated SNR' of the frames added fell by more than 10% of the calculated SNR' from the previous iteration. Percentages of side slither length were chosen in 5% intervals as processing power was limited. A decrease in SNR' of 10% was chosen because a decrease

of less than 10%, i.e. 1-9%, prevented the frame number from growing beyond 5%. A decrease in SNR' greater than 10% allowed for noisy regions of the signal to be chosen and negatively impacted the relative gains. Due to only uniform regions being used as a target for the side slither maneuver, all following FPMs after FPM 1 should have the same highest uniform region; therefore, uniform frame selection was only completed for the first FPM in each band for each side slither.

3.3.3. FPM to FPM Correlation

The spatial separation between FPMs creates a shift in the selected uniform region that needs to be accounted for to have all FPMs to view the same locations of the Earth. To account for the shift in the selected uniform region the number of frames that each FPM is shifted beyond the first FPM needs to be calculated. First, the variance of each frame within the side slither data was calculated for each FPM. Then, the variance data of the second FPM was cross correlated to the variance data of the first FPM and the max value of the cross-correlation output determined the number of frames shifted between the first and second FPMs. The basics of the cross-correlation function are explained in further detail by Paul Bourke [17]. The frame shift between the first and third FPMs was then calculated in the same way. However, due to the nature of even and odd FPMs being spatially different than each other when the sensor is rotated in the yaw direction, the remaining even FPMs, FPMs 4-14, were cross correlated with FPM 2 and the shift between FPM 1 and FPM 2 was added to their result. The remaining odd FPMs, FPMs 3-13, were cross correlated with FPM 1 in the same manner. With the frame shift between FPMs calculated, the same highly uniform region of Earths surface could be selected within each FPM to derive the ideal

relative gains. Figure 8 shows the DN value vs frames of the side slither and how the region used for relative gain derivation needs to be shifted to acquire the same region on the Earth when comparing FPM 1 and FPM 14. The frame shift values for each FPM differed between side slither locations, so FPM shift values were calculated for each of the three locations, saved, and applied to all future side slithers that were taken in the same location, i.e. Greenland FPM shifts were applied to future Greenland side slithers.

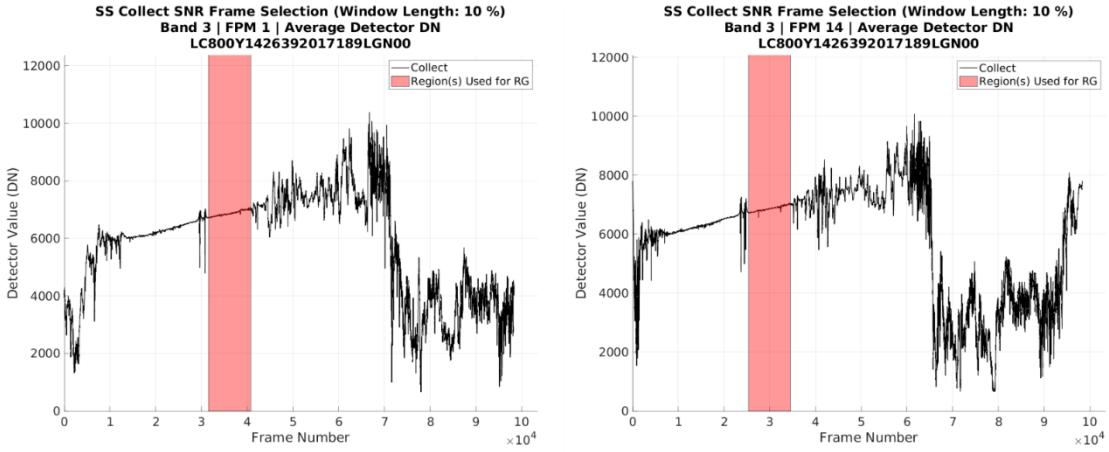

Figure 8. Band 3 FPM 1 region used for relative gains (left) compared to FPM 14 region used for relative gain derivation (right) from same Greenland Side Slither.

The layout of Landsat 8 FPMs, as shown in Figure 3, causes even and odd FPMs to detect different portions on the ground during the side slither maneuver. However, uniform regions are used to mitigate this problem, and it is assumed that the difference between measured portions of the Earth are negligible.

3.3.4. Detector Relative Gain Calculation

Relative gains for each detector within each FPM can be calculated from the highly uniform regions selected through the FPM-to-FPM correlation algorithm. To calculate relative gains equation 5 is used,

$$RG_i = \overline{DN}_{Li}/\overline{DN}_L \quad (5)$$

where RG_i is the relative gain for the ith detector, $\overline{DN}_{Li}$ is the average linearized DN value across all frames for the ith detector, and $\overline{DN}_L$ is the average linearized DN value for all detectors within an FPM across all frames. Detector Relative gains are then applied to each bias subtracted detector within a scene to align each detector using equation 6,

$$L_i = DN_{bi}/RG_i \quad (6)$$

where L_i is the corrected data in DN for the ith detector, DN_{bi} is the bias subtracted data for the ith detector, and RG_i is the detector relative gain for the ith detector.

3.3.5. FPM Relative Gain Calculation

Relative gains for each FPM are calculated in a similar way to the detector gains, however, FPM relative gains are meant to align differences between FPMs. Thus, to calculate FPM relative gains the following equation 7 was used,

$$G_j = \overline{DN}_{Lj}/\overline{DN}_L \quad (7)$$

where G_j is the FPM to FPM gain for the jth FPM, $\overline{DN}_{Lj}$ is the average linearized DN value for the jth FPM across all frames, and $\overline{DN}_L$ is the average linearized DN value across all frames selected for all FPMs. FPM relative gains are calculated for the jth FPM and are then applied to each detector within jth FPM. FPM relative gains are applied to each bias

subtracted scene to align each FPM radiometrically. FPM 1 is used as the reference FPM for calculation of rest of the FPM gains within the same band.

3.4. Scene Selection

For the purposes of validating the improvement in the detector and FPM relative gains, 7 different scene sets were selected. The first two scene sets were from Antarctica and Greenland, where each image was located over ice and snow and taken from the time of Landsat 8's launch through December 2019. Antarctica and Greenland land cover was chosen as they are bright in the UV-Vis bands and are highly uniform; therefore, removing most scene effects when attempting to measure Streaking Metrics. However, Antarctica scenes could only be acquired in the months of October to March, and Greenland scenes in the months of April to September, as the sun does not provide enough signal outside those seasonal time intervals.

The third, fourth, and fifth data sets were chosen based on high uniformity and signal in the SWIR bands. These data sets are located in the Arabian Desert, Northeast Africa, and Australian desert respectively. Each desert image was inspected for clouds and selected based on high spatial uniformity, therefore removing potential scene effects from the Streaking Metric.

The sixth and seventh data sets were taken from the Mediterranean Sea and the Amazon Rain Forest, respectively. Both these data sets are dark within the UV-SWIR wavelengths, however, in the TIRS wavelengths they provide highly uniform regions and were designated to explore the extent of streaking reduction when side slither relative gains were applied to low signal areas.

Table 4 shows the number of scenes in each data set as well as the path/row range for each data set and the main wavelengths of interest with each data set. All scenes used were Level 0 images acquired by Landsat 8 and downloaded through the Earth Explorer interface.

Table 4. Summary of scene locations used for side slither comparison

Location	Number of Scenes	Path/Row Range	L8 Bands of Interest
Greenland	114	P7-P32; R2-R5	1-5; 8; 10-11
Mediterranean Sea	32	P185-P188; R34-R37	1-3; 10-11
Arabian Desert	179	P162; R46	1-8; 10-11
Australian Outback	41	P100; R77	1-8; 10-11
North African Desert	46	P181; R40	1-8; 10-11
Amazon Rain Forest	173	P1; R65	1-8; 10-11
Antarctica	120	P106-P174; R115-R121	1-5; 8; 10-11

3.5. Other Methods of FPM Gain Estimation

Throughout the process of developing the side slither relative gain derivation algorithm, other methods for relative FPM correction were produced. Chief among these new processes are an in-scene estimation method and a periodic model estimation method. These new methods are important as they provide an alternative method of calibration should something go wrong with an operational approach and can be applied to almost all push broom scanners.

3.5.1. In-Scene Estimation

Since each FPM is essentially a separate imaging system, the noise and offset of each FPM is unique. To determine how each FPM's noise and offset relate to the others, approximately 25 detectors within each FPM were built such that they overlap with the neighboring FPM's 25 detectors. For each scene individually, these overlap detectors were

used to characterize differences between FPM's and to correct each FPM. The average signal level of the 25 overlap detectors from the first FPM were calculated and divided by the average of the overlap detectors from FPM 2. Overlap ratios were found for each neighboring FPM pair resulting in 13 different ratio values. Setting FPM 1 as the reference FPM, i.e. the FPM relative gain for FPM 1 is set to unity, the gains for each following FPM were calculated by multiplying the overlap ratio by the previous FPM gain to create a uniform image across all FPMs. Example calculations of FPM relative gains for FPM 2 and 3 can be found in equation 8 and equation 9 respectively,

$$FPM_2 = 1 * Ratio_{12} \tag{8}$$

$$FPM_3 = FPM_2 * Ratio_{23} \tag{9}$$

where FPM is the FPM relative gain, and Ratio is the overlap of the 25 detectors between FPMs 1 and 2 for $Ratio_{12}$ and FPMs 2 and 3 for $Ratio_{23}$. The 14 different in-scene FPM gains were then normalized to a value of 1 to sustain the integrity of the radiometric calibration of the instrument.

3.5.2. Periodic Model Estimation

A supplemental form of FPM relative gain correction was developed based on a periodic model estimation. As an example, the in-scene estimated FPM gain values for all the Arabian Desert images available from Landsat 8 using the overlap detectors between FPMs were graphed over a timeline to determine how the FPM gain changed over time. Outliers within the timeline were found and removed through the use of a Hampel filter to reduce major changes in FPM relative gains that were typically caused by clouds [18].

Figure 10 shows the timeline for the relative gain of Band 1 FPM 1 with cloudy outliers removed.

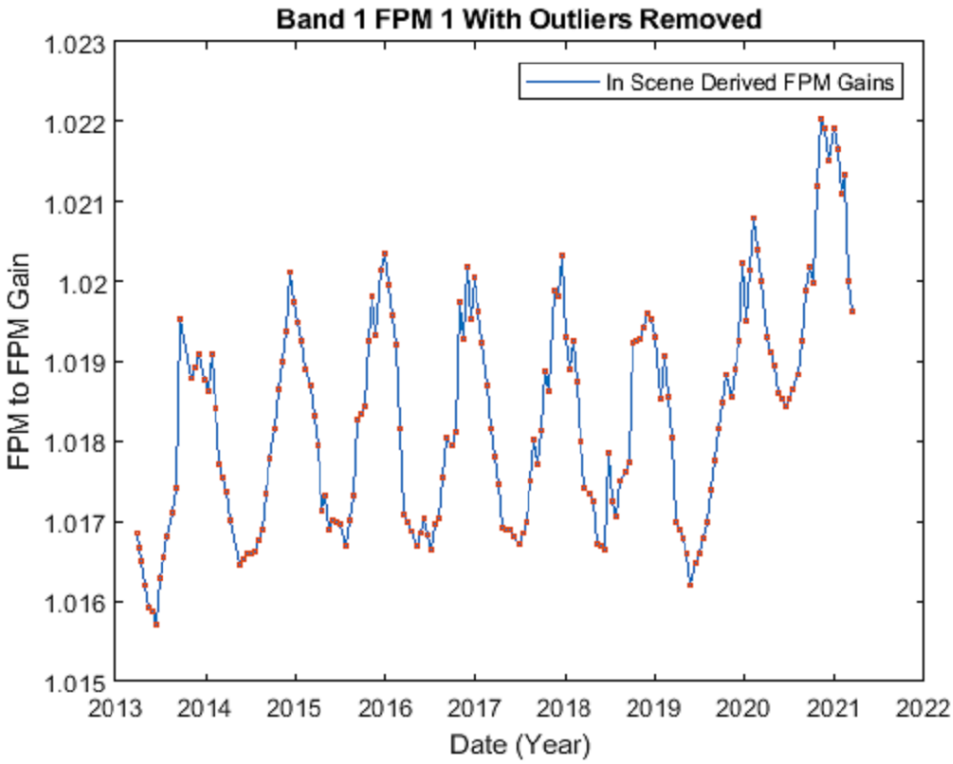

Figure 10: In-scene FPM relative gain for Band 1 FPM 1 across all Arabian Desert scenes through Landsat 8's lifetime.

Based on the timeline, a yearly periodic plus a linear trend was observed. A true sinusoid plus linear model was fitted to the data; however, the sinusoid could not encapsulate the extreme rise and falls of the FPM to FPM gains while attaining the same period as the data timeline. To attempt to recreate the temporal data trend, a linear regression was fit to the data. Data from the year 2017 to 2018 was replicated to create the yearly trend on the data, as this year was the highest sampled year from the Arabian Desert scenes. To determine the yearly trend, the difference between the linear regression line and the data points in the year 2017 to 2018 were calculated. The differences between the data

and the linear regression were then added to the linear regression line in a yearly fashion to create a periodic model based on the 2017 to 2018 data as shown in Figure 11.

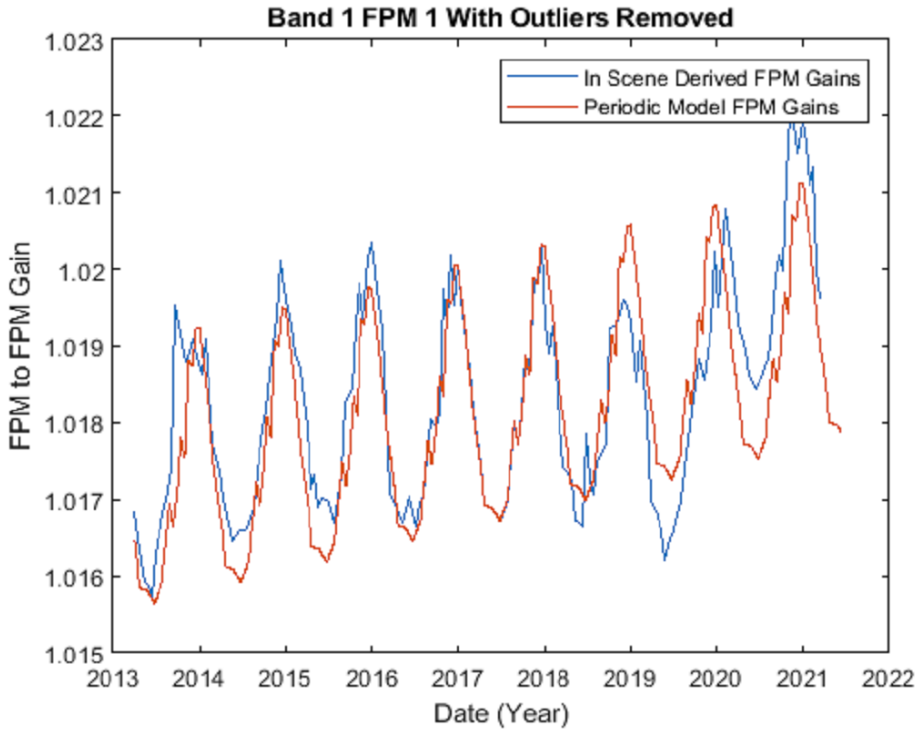

Figure 11. In-scene derived FPM Gains for Band 1 FPM 1 from Arabian Desert scenes (blue) compared to periodic model FPM gains (red) graphed across Landsat 8's lifetime. Each of the 14 FPMs will have a model similar to this and some are positively linear while others are negatively linear.

Each band and FPM underwent a fitting in this way and an FPM gain was calculated for each day of the year through linear interpolation of the periodic model. The periodic model provides a method to track FPM relative gain changes throughout the year and provide near perfect gains, when compared to the in-scene relative gains, for every day and can be acquired with, at minimum, a year's worth of data. This model also provides a method of FPM calibration that can be tracked and have a specific value over time as opposed to in-scene correction, which can vary greatly scene by scene, invalidating the

integrity of the radiometric calibration of the instrument. From a consistent calibration perspective, the periodic model provides a stable FPM gain value through time as the model is derived one time, and can be used throughout the lifetime of the instrument. Analysis into the relevancy of the periodic model over the lifetime of Landsat 8 and application will be explored in detail in Section 4.2.

3.6. Evaluation Metrics

Statistical methods were used to compare which relative gain estimation method had a greater effect on removing the differences between detectors and FPMs. For measuring the differences between relative detector gains, the Streaking Metric statistically compares the deviations between adjacent detectors and can be used to measure a relative gain's ability to remove said dissimilarities between detectors. To compare FPM correction methods, the Overlap Detector Metric was created to statistically determine how far away from the perfect detector overlap ratio of 1 each FPM correction method could achieve.

3.6.1. Streaking Metrics

The Streaking Metric, as defined by the Landsat 8 ADD [12], is used to statistically find differences between detectors in what should be a uniform image. The streaking can be calculated by equation 10,

$$S_i = |\bar{L}_i - 0.5 * (\bar{L}_{i-1} + \bar{L}_{i+1})|/\bar{L}_i \quad (10)$$

where S_i is the Streaking Metric per detector, $\bar{L}_i$ is the mean of a detector column in a validation image, and i is the detector column number. A lower streaking metric indicates

a smaller difference between neighboring detectors, therefore, the smaller the streaking metric the better the relative detector gains are.

3.6.2. Overlap Detector Metric

Overlap detectors between adjacent FPMs provide a unique opportunity to assess the performance of FPM relative gain estimation. Since, over level terrain, these detectors view nearly identical locations of the Earth's surface, any deviation from identical values is a measure of degraded performance for the FPM relative gains. This approach is quantified in equation 11 by,

$$R_j = |1 - (\overline{DN}_j / \overline{DN}_{j+1})| \tag{11}$$

where R_j is the overlap ratio of the jth FPM, DN_j is the average of the jth FPM overlap detectors, and j is the FPM. To determine whether the differences between CPF, modeled overlap, and SS overlap metrics were statistically significant, a student's t-test was used. The student's two sample two sided t-test with a significance level of 0.05 was applied to each average of overlap metric within each scene set where a rejection of the null hypothesis resulted in statistically different averages. A lower Overlap Detector Metric indicates a smaller difference between neighboring FPMs, therefore, the smaller the Overlap Detector Metric the better the relative FPM gains are.

3.7. Side Slither Selection for Scene Type

To determine how to acquire the lowest Streaking Metrics, the best locations for side slithers for each band needed to be determined. Relative gains derived from the three

locations, Greenland, North Africa, and Antarctica, were tested on all the scene sites and the best side slither for each band was determined.

3.7.1. Best SS Location per Band

For the VNIR wavelengths, a comparison of Streaking Metrics between a Greenland, North Africa, and Antarctic side slither resulted in the Greenland and Antarctic side slithers producing the lowest Streaking Metrics on average. Greenland and Antarctica produced better relative gains compared to North Africa due to snow and ice, the majority land cover type for polar side slithers, having a better signal-to-noise ratio within the VNIR bands when compared to sand, the majority land cover type of North African side slithers. While the Antarctic side slither produced relatively low Streaking Metrics, the Greenland side slither tended to yield overall lower Streaking Metric averages over all images. Figure 12 shows a visual comparison between two different side slither locations applied to the same Greenland scene and how the Greenland relative gains are more efficient in removing vertical stripes, i.e. streaking, from the image compared to the North African relative gains. It should be noted that the Greenland relative gains are not derived from the same location that the Greenland scene was acquired. The Greenland scene was used because of the high uniformity present in snow covered scenes, creating a scene in which the detector level striping can be noticeable.

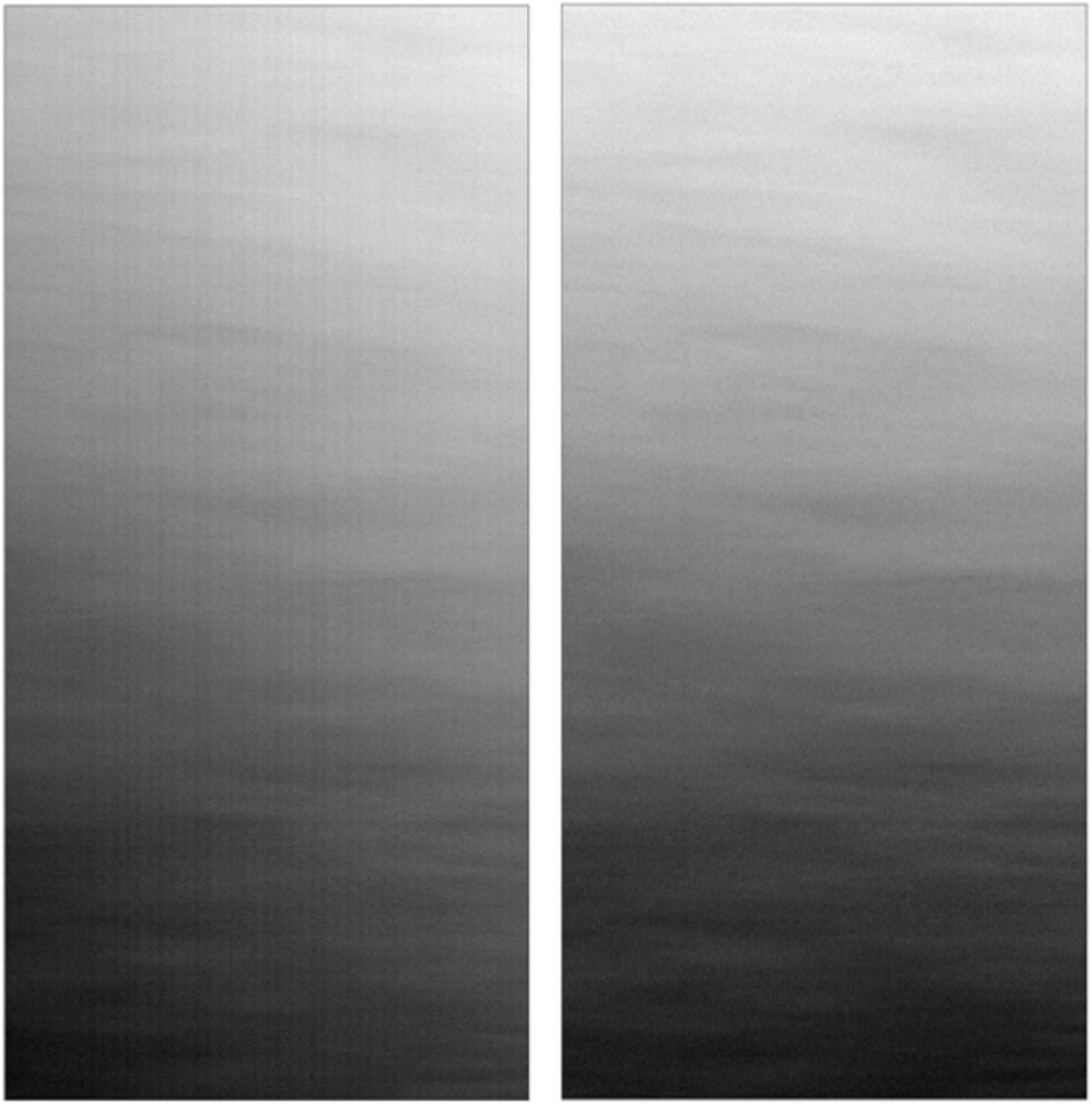

Figure 12. North Africa side slither relative gains for the C/A band applied to FPM 2 of a Greenland Scene (left) ; Greenland side slither relative gains for the C/A band applied to FPM 2 of a Greenland scene (right). These two images have an identical contrast stretch applied to them for visualization purposes. Note the large amount of vertical stripes visible in the left image vs the right image.

For the SWIR bands, the same comparison of Streaking Metrics between side slithers was produced. Overall, when images with a normal to above average signal in the SWIR bands such as vegetation, sand, and soil, the North African side slithers produced the lowest Streaking Metrics. When images with below average signal such as water, ice,

and snow, the best side slither to use was a deadlock as noise was the driving factor behind the Streaking Metrics in those images. Due to the North African side slither deriving relative gains from sand, which has a larger signal to noise ratio for SWIR bands when compared to ice and snow, the Streaking Metrics from the North African side slither are statistically better than those of Greenland and Antarctic relative gains in the SWIR bands.

For the thermal infrared (TIRS) bands, i.e. bands 10 and 11, the best relative gains depended primarily upon the signal strength of the image compared to that of the side slither. For colder scenes such as those from high latitude regions, the cold side slithers from Greenland and Antarctica provided lower Streaking Metrics; however, for warmer scenes like those from any of the other scene sets, the North African side slithers provided lower Streaking Metrics.

Relative detector gains derived from each location were applied to each scene set and a summary of the Streaking Metrics were created using a per scene average. Table 5 shows the summary of the average Streaking Metrics for each side slither applied to all scenes. To compare method averages a two-sample two-sided t-test with a significance level of 0.05 was performed two side slither location's streaking band averages to determine statistical differences between each method. Streaking Metrics for individual scene sets can be found in Appendix A, Table A1.

Table 5. Summary of scene average Streaking Metrics for three separate SS locations; red data is statistically the worst, followed by yellow data, and green data is statistically the best; if multiple cells are the same color that data is statistically equal as proven by the t-test.

Band	Antarctic SS Y2019 D015 (μDN)	Greenland SS Y2019 D195 (μDN)	N. Africa SS Y2018 D290 (μDN)
C/A	396	347	408
Blue	363	341	500
Green	356	333	401
Red	445	381	403
NIR	387	389	452
SWIR-1	1,509	1,292	976
SWIR-2	979	1191	957
PAN	383	344	463
TIRS-1	3,551	2,628	2,792
TIRS-2	6,008	5,032	6,369

Based on these Streaking Metrics and the Streaking Metrics located in the Appendix, the best side slither locations for each band were chosen. Figure 13 shows a flowchart for the best side slither location for each band as determined through the Streaking Metrics, where the lowest Streaking Metrics account for the best side slither.

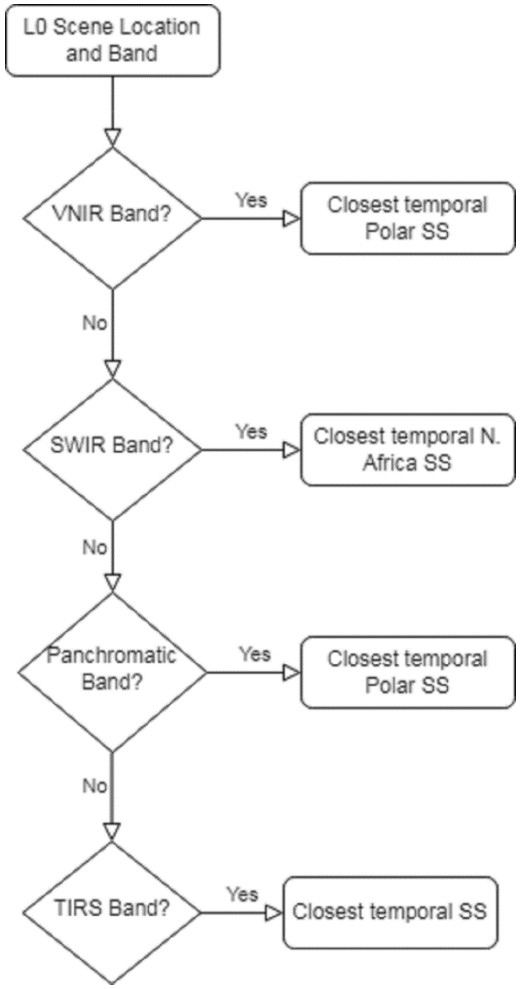

Figure 13. Flowchart for determining which side slither to use based on band

3.7.2. Temporal Integrity of SS relative gains

Currently, Landsat 8 takes a side slither from each of the three sites once a year according to standard operating procedures developed by USGS EROS. To determine whether acquiring side slither data once a year was the ideal frequency, it needed to be determined how long each individual side slither's relative gain set was useful for as the detectors will change temporally, rendering the relative gains impractical. For comparison, CPF files create new relative gains every three months; however, acquiring Greenland, North African, and Antarctic side slithers every three months or less was not feasible for multiple reasons. Greenland side slithers were not acquired at a rate greater than yearly

because Greenland can only be imaged 6 months out of the year due to low sun angles. Antarctic side slithers suffer from the same imaging limitation with the opposite 6 months as Greenland. North African side slithers were not acquired greater than a yearly rate because Central Africa is an area of great interest for Landsat imaging and when a side slither is performed, normal imaging cannot occur again over most of the African continent. Side slithers in Greenland and Antarctica also incapacitate normal imaging at the time of acquisition and for many scenes following; however, due to the extreme latitudes, many path/rows overlap and the region of land used for side slither will be imaged again sooner compared to those used in North Africa.

To establish the useful lifetime of a side slither relative gain, the relative gains from a North African side slither were applied to various North African scenes ranging in date from 2013, the launch date of Landsat 8, to August of 2020. Once the North African side slither relative gains were applied to the North African scenes, the average Streaking Metric for each scene was calculated and plotted temporally. To compare to CPF relative gains, the CPF relative gains acquired temporally closest to the side slither date was also applied to each of the same scenes. Figure 14 shows the Streaking Metric average of each scene graphed over time for side slither relative gains compared to the CPF relative gains. Based on Figure 14 the side slither relative gains tend to have a longer lifetime than those of the CPF relative gains as shown by the values of the SS Streaking Metrics away from the date of the SS (as indicated by the vertical black line on the plot. The side slither Streaking Metric averages are better than that of the CPF for at least a year on either side of the acquisition date. Therefore, acquiring one side slither of each type once a year is

enough to satisfy relative detector calibration. However, using the side slither relative gain set temporally closest to the time of scene acquisition for the specified bands above results in minimizing the Streaking Metric.

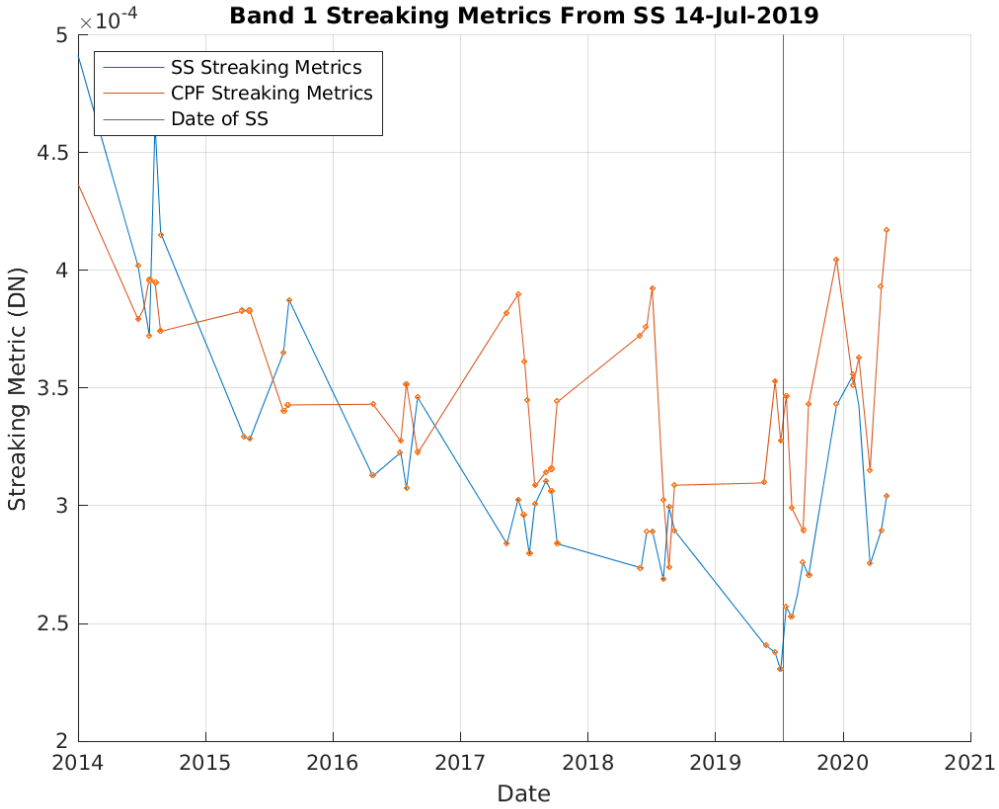

Figure 14. Timeline of Streaking Metric averages for Greenland side slither relative gains (Y2019 D195) applied to all North Africa scenes compared to CPF relative gains Streaking Metric averages applied to the same scenes.

4. RESULTS AND DISCUSSION

The following results are divided into two focus areas: qualitative and quantitative. Since relative gain errors always result in streaking and striping, a visual assessment of the imagery provides an intuitive evaluation of the algorithm performance from a qualitative

perspective. Additionally, quantitative metrics, which are related to visual evaluation, provide a firm measure for algorithm optimization and comparisons.

4.1 Detector Relative Gain Comparison

As the current method of relative gain derivation is derived from the diffuser method and stored in the CPF, it is paramount that side slither relative gains are compared to current primary methods. To achieve this comparison both CPF relative detector gains and side slither relative detector gains were applied to all validation scene sets. The SS and CPF relative gains were applied to each scene set and a summary of the statistics were created using a per scene average. Table 6 provides a summary of each band's Streaking Metric for all scenes when side slither and operational CPF relative detector gains were applied. To compare method average's a two-sample two-sided t-test with a significance level of 0.05 was performed on SS and CPF streaking band averages to determine statistical differences between each method. Complete Streaking Metrics applied to all scene sets can be found in Appendix A Table A2.

Table 6. Average Streaking Metrics when the best SS relative gain set is applied to Arabian desert scenes and compared to operational CPF relative gain sets; yellow cells contain statistically worse data than green cells; if multiple cells are the same color that data is statistically equal as proven by the t-test.

Band	CPF Streaking Average (μDN)	SS Streaking Average (μDN)
C/A	575.7	488.9
Blue	721.0	571.0
Green	493.6	434.2
Red	406.5	406.8
NIR	360.8	366.1
SWIR-1	845.4	1,268
SWIR-2	822.6	1,164
PAN	387.6	350.0
TIRS-1	1,058	764.5
TIRS-2	639.1	409.2

Overall, side slither compares well with CPF Streaking Metrics, with side slither outperforming the CPF relative detector gains in bands 1-3 (C/A through Green) and 10-11 (TIRS-1 through TIRS-2). On the other hand, CPF relative detector gains outperform the SS in bands 5-7 (NIR through SWIR2), and SS and CPF perform equally as well in the red band. Though these values may be statistically different, all Streaking Metric values shown are well below the required Streaking Metric set by USGS of 5 mDN, indicating that both methods provide adequate relative detector gains.

4.2. FPM Relative Gain Comparison

Similar to detector relative gains, the relative FPM gains must be compared to current methods to determine whether there is comparable or improved performance. For the relative FPM gain comparison three methods were compared, CPF (current method

from diffuser), side slither, and the periodic model (derived from in-scene corrections). The in-scene method is not compared here because, based on the metric used, the in-scene values would have a perfect metric of zero as each scene has its own calculation. While in-scene relative FPM corrections provide a perfect scene from a statistical standpoint, from a radiometric standpoint the calibration would not be consistent across all scenes thus rendering the in-scene relative FPM correction impractical. The relative FPM gains for each method were applied to each validation scene set and a summary of the statistics were created using a per scene average. Table 7 shows the comparison between relative FPM gains corrections based on the Overlap Detector Metric when applied to all scenes sets. To compare method averages, a two-sample two sided t-test with a significance level of 0.05 was performed on two methods at a time to determine statistical differences between each method. Complete FPM to FPM gain comparison averages for each scene type can be found in Appendix A, Table A3.

Table 7. Summary of average Overlap Detector Metric for all scene sets from the three FPM gain correction methods; red data is statistically the worst, followed by yellow data, and green data is statistically the best; if multiple cells are the same color that data is statistically the same as proven by the t-test. In-scene metrics are not shown as their value would be 0 due to being derived from the scene itself.

Band	CPF (10^{-3})	Periodic Model (10^{-3})	Nearest SS (10^{-3})
C/A	3.93	3.39	3.60
Blue	4.52	4.13	4.35
Green	5.13	4.79	5.34
Red	5.97	5.63	6.34
NIR	3.13	2.88	3.76
SWIR-1	15.1	14.6	16.4
SWIR-2	19.7	19.2	20.3
PAN	3.57	3.12	4.16
TIRS-1	11.1	6.19	16.5
TIRS-2	29.4	9.03	15.6

Overall, the periodic model provides the best relative FPM gains when quantitatively compared to the CPF and SS relative FPM gains. The CPF FPM gains produce the second best relative FPM gains and SS generated the least effective method for relative FPM correction. To qualitatively compare each method of FPM correction, the best and worst scenes in terms of FPM correction were found. The best scene for FPM correction, Figure 15 has a large range of pixel values reducing the ability to see differences between FPMs. Figure 15 shows a contrast stretched and zoomed-in image from the Australian desert focused on an FPM boundary where all four methods of FPM correction produce almost exactly the same image.

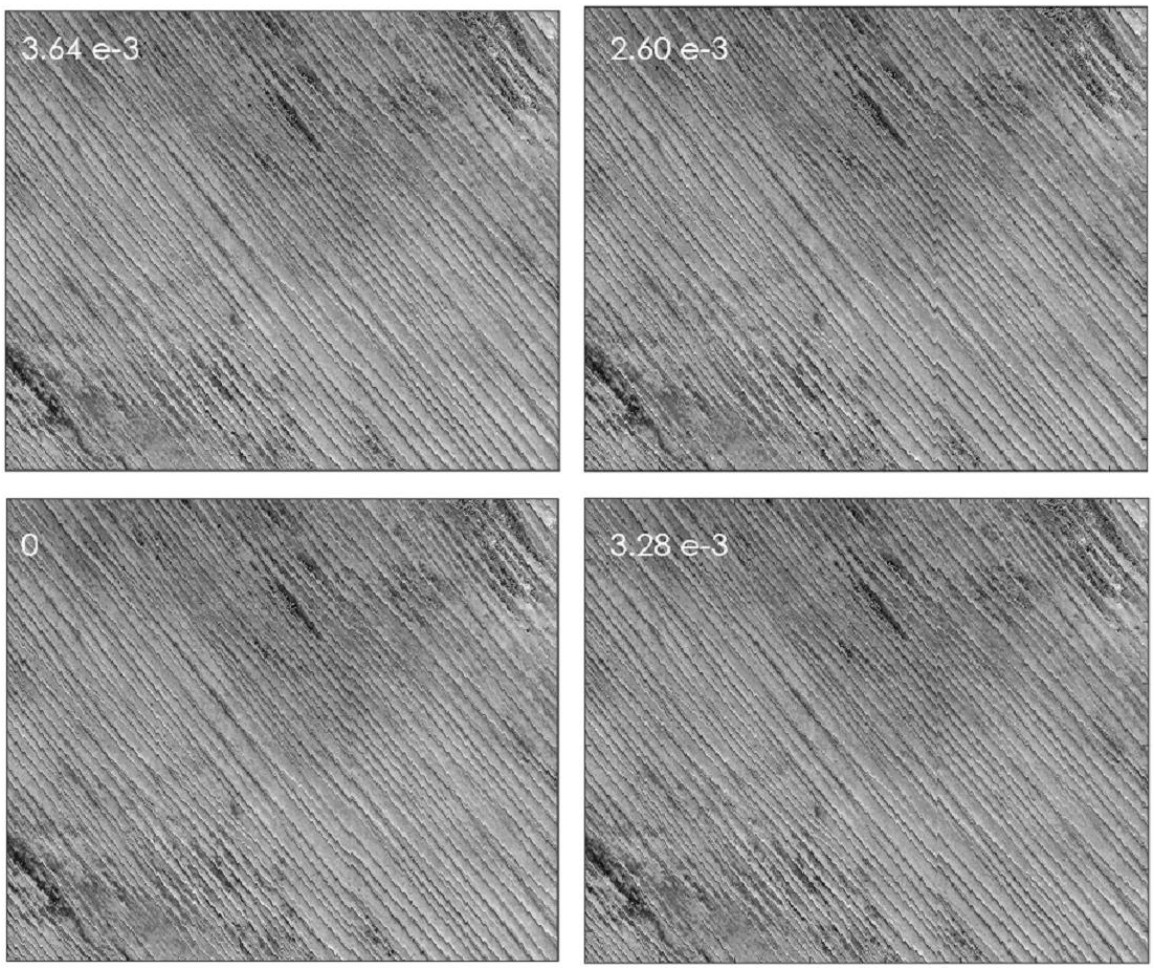

Figure 15. Contrast stretched and zoomed-in band 5 Australian Desert image with: SS FPM gains Applied (Top Left); CPF FPM gains Applied (Top Right); In-Scene FPM gains Applied (Bottom Left); Modeled FPM gains Applied (Bottom Right). In the top left corner of each scene is the overlap detector metric for that scene.

From this group of images it can be seen that there are no visible differences between the left portion of the FPM boundary and the right portion of the FPM boundary. Quantitatively, the CPF FPM correction performs the best followed by the modeled FPM values. The side slither FPM gains perform the worst, relatively. Overall, each method of FPM correction shown qualitatively improves this specific scene to the same point.

The worst case scene for FPM correction has a small pixel range allowing the viewer to see the distinct differences between FPMs. Figure 16 shows a contrast stretched image of the Mediterranean Sea with all four methods applied to the same scene. The FPM boundaries qualitatively portray how effective each FPM correction method is at normalizing each FPM.

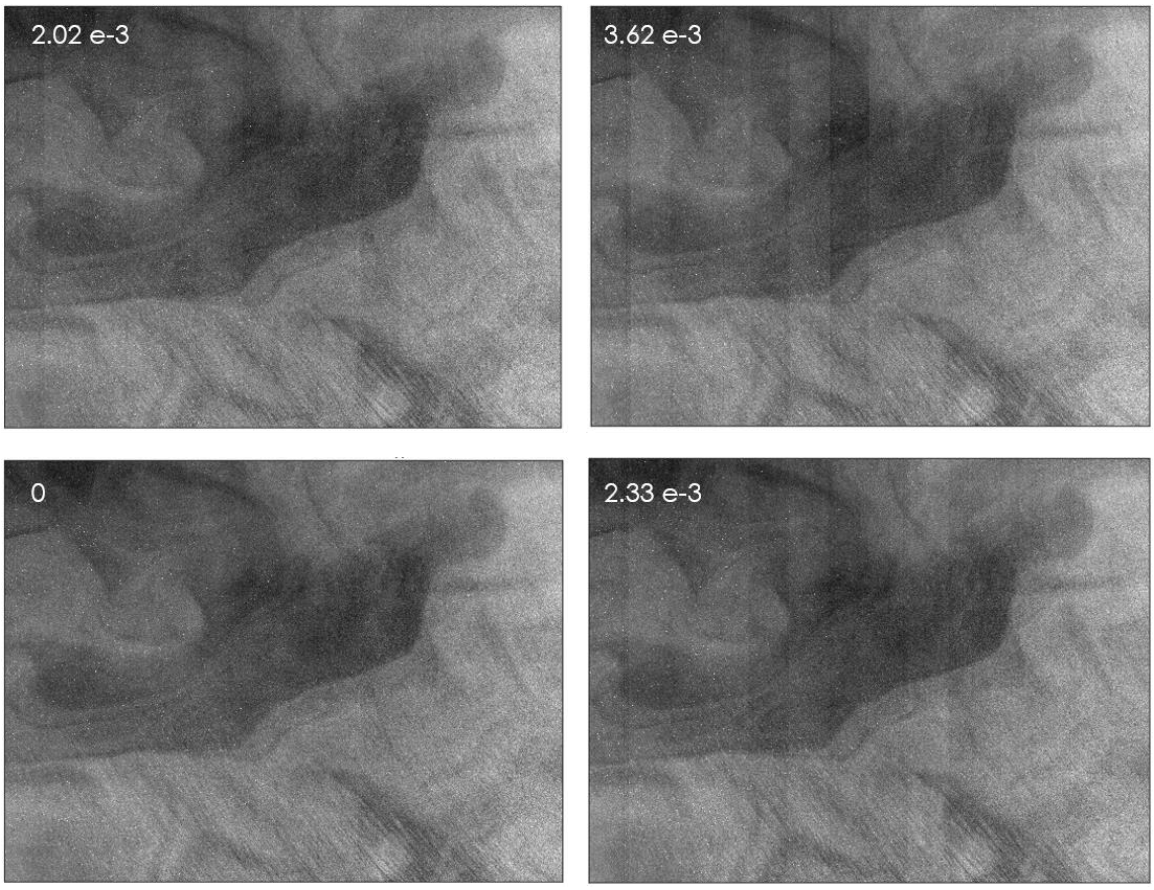

Figure 16. Contrast stretched band 1 Mediterranean Sea image with: SS FPM gains Applied (Top Left); CPF FPM gains Applied (Top Right); In-Scene FPM gains Applied (Bottom Left); Modeled FPM gains Applied (Bottom Right). In the top left corner of each scene is the overlap detector metric for that scene.

Qualitatively, it can be seen that in-scene FPM to FPM correction provides the best correction to this specific scene as there are no visible FPM boundaries within the scene.

The modeled and side slither FPM gains provide the next best FPM correction, as shown by both the image and metric, and CPF provides the worst FPM correction. However, all four methods provide a correction that could be applied to visually correct relative FPM differences amongst any pushbroom scanner images. Quantitatively, the periodic model provides the best relative FPM correction without using in-scene detectors to correct an image and is the suggested method for FPM correction.

5. CONCLUSION

Though the side slither technique has been around for nearly two decades now, the usage and methodology surrounding side slithers remains limited. This study sought to resolve some of the issues remaining with side slither and provide a quality method to derive relative gains for all pushbroom scanning satellites.

The optimal side slither was chosen through two stipulations. First, the best side slither to use for relative gain correction was determined to be the temporally closest to the acquisition date of the image being corrected. Second, for VNIR bands Greenland provided the best relative gains, for SWIR bands the North Africa side slither provided the optimal gains, and for thermal bands both Greenland and North Africa provided comparable relative gains depending on signal strength within the image.

Although CPF relative gains derived from the diffuser method already provide a large reduction in streaking within the image, not all missions have them. Also, diffuser panels can degrade; therefore, side slither provides a functional alternative with a comparably high level of streaking reduction. When directly compared to the CPF values, side slither relative detector gain values even outperform those of the CPF values in the

C/A, blue, green, and thermal bands. However, due to the non-uniformities in the North African side slithers, the Streaking Metric reduction will underperform when compared to CPF relative gains for the SWIR bands. Side slither relative gain sets from Landsat 8 suffer from low frequency acquisition as the maneuver interrupts normal imaging. This lack of data acquisition can be a problem if a detector were to degrade rapidly with respect to side slither acquisitions. However, a yearly acquisition of relative gains provide an average Streaking Metric within scenes to meet the Landsat 8 standard as described in the ADD. In the future, methods of relative gain interpolation may be designed to account for the low frequency acquisitions.

For FPM relative gains, using the overlap detectors within a scene to calculate the FPM relative gain correction will remove all banding between FPMs both qualitatively and quantitatively. However, radiometrically it is applying a scene-specific correction to each scene that cannot be justified from a consistent calibration perspective. Therefore, the periodic model based on in-scene FPM relative gain values from the Arabian Desert provide the best FPM correction gains while sustaining the integrity of radiometric calibration. Second to the periodic model FPM relative gains are the CPF FPM relative gains which is the current standard for relative gains, followed by the side slither FPM relative gains on average.

Overall, side slither provides relative gain sets that both qualitatively and quantitatively remove streaking between detectors and banding between FPMs, and, at times, exceeds the streaking reduction of current operational methods. The side slither procedure performs well compared to the diffuser method such that it provides not only a

backup to current operational approaches, but could also serve as a primary method of relative gain estimation for any pushbroom sensors.

APPENDIX

Appendix A.1.

Table A1. Full table of Streaking Metric comparisons; red data is statistically the worst, followed by yellow data, and green data is statistically the best; if multiple cells are the same color that data is statistically the same as proven by the t-test.

	Antarctica Snow Scenes			Australian Desert Scenes		
Band	Antarctic SS Y2019 D015 (µDN)	Greenland SS Y2019 D195 (µDN)	N. Africa SS Y2018 D290 (µDN)	Antarctic SS Y2019 D015 (µDN)	Greenland SS Y2019 D195 (µDN)	N. Africa SS Y2018 D290 (µDN)
C/A	351	454	620	373	370	447
Blue	292	401	725	307	346	579
Green	251	307	458	319	305	364
Red	276	167	214	389	315	322
NIR	156	177	286	273	291	347
SWIR-1	1,567	1,198	1,092	1,367	1,217	634
SWIR-2	774	1,033	904	767	1,030	594
PAN	230	211	505	418	358	283
TIRS-1	1,054	2,880	5,559	4,889	2,830	1,541
TIRS-2	2,476	5,236	9,727	8,225	5,673	5,029
	Amazon Forest Scenes			N. African Desert Scenes		
Band	Antarctic SS Y2019 D015 (µDN)	Greenland SS Y2019 D195 (µDN)	N. Africa SS Y2018 D290 (µDN)	Antarctic SS Y2019 D015 (µDN)	Greenland SS Y2019 D195 (µDN)	N. Africa SS Y2018 D290 (µDN)
C/A	402	394	457	450	340	365
Blue	376	429	655	388	339	451
Green	556	576	634	371	324	367
Red	908	878	879	363	315	339
NIR	908	913	934	318	290	353
SWIR-1	1,699	1,488	1,222	1,358	1,257	632
SWIR-2	1,530	1,710	1,530	795	1,041	562
PAN	607	588	806	341	297	305
TIRS-1	4,279	2,281	1,784	4,989	2,935	1,440
TIRS-2	7,688	5,298	5,618	8,121	5,613	4,875
	Greenland Snow Scenes			Arabian Desert Scenes		
Band	Antarctic SS Y2019 D015 (µDN)	Greenland SS Y2019 D195 (µDN)	N. Africa SS Y2018 D290 (µDN)	Antarctic SS Y2019 D015 (µDN)	Greenland SS Y2019 D195 (µDN)	N. Africa SS Y2018 D290 (µDN)
C/A	335	233	251	395	302	338
Blue	337	260	269	327	278	393
Green	222	182	226	290	219	281
Red	261	153	189	304	206	243
NIR	147	164	249	234	220	290
SWIR-1	1,636	1,164	1,126	1341	1241	598
SWIR-2	809	1,038	937	759	1031	538
PAN	223	196	331	357	288	253
TIRS-1	1,418	1,423	4,043	5,052	2,968	1,456
TIRS-2	2,023	2,683	7,733	7,896	5,254	4,522

Table A2. Complete table of CPF to SS Streaking Metric comparison; yellow cells contain statistically worse data than green cells; if multiple cells are the same color that data is statistically equal as proven by the t-test.

	Antarctica Snow Scenes		Greenland Snow Scenes	
Band	CPF Streaking Average (µDN)	SS Streaking Average (µDN)	CPF Streaking Average (µDN)	SS Streaking Average (µDN)
C/A	733.6	687.7	319.1	201.3
Blue	751.3	613.0	345.6	190.2
Green	466.1	414.1	238.2	157.9
Red	185.5	192.1	156.8	156.1
NIR	230.9	242.3	159.5	169.5
SWIR-1	997.2	1,317.9	1,031.9	1,246.9
SWIR-2	755.1	1,066.1	826.5	939.9
PAN	426.2	366.0	292.1	234.4
TIRS-1	2389	1,587	1,451	647.9
TIRS-2	771.0	562.5	696.0	329.6
	Mediterranean Sea Scenes		Australian Desert Scenes	
Band	CPF Streaking Average (µDN)	SS Streaking Average (µDN)	CPF Streaking Average (µDN)	SS Streaking Average (µDN)
C/A	499.2	399.1	656.0	565.1
Blue	528.5	345.6	798.3	630.9
Green	631.0	570.3	490.2	427.9
Red	841.1	837.5	478.2	479.6
NIR	1,532.1	1,529.3	308.9	315.3
SWIR-1	3,400.7	3,633.9	440.9	1,037.7
SWIR-2	3474.3	3,614.7	409.2	919.3
PAN	900.6	844.2	310.3	305.7
TIRS-1	407.6	474.6	559.1	392.3
TIRS-2	520.8	386.2	569.9	332.1
	N. African Desert Scenes		Amazon Forest Scenes	
Band	CPF Streaking Average (µDN)	SS Streaking Average (µDN)	CPF Streaking Average (µDN)	SS Streaking Average (µDN)
C/A	503.3	396.8	733.2	649.4
Blue	642.7	475.3	907.8	762.0
Green	374.9	322.2	793.5	745.0
Red	290.1	287.9	881.4	880.8
NIR	283.0	282.3	567.3	570.1
SWIR-1	380.2	906.1	845.7	1,272.7
SWIR-2	350.9	795.6	1,083.0	1,401.8
PAN	378.1	378.6	552.8	497.1
TIRS-1	624.0	423.6	701.9	843.9
TIRS-2	607.1	355.3	604.2	458.3

Band	Arabian Desert Scenes CPF Streaking Average (µDN)	SS Streaking Average (µDN)
C/A	495.0	405.8
Blue	796.1	652.1
Green	391.4	329.3
Red	190.4	189.2
NIR	199.1	202.3
SWIR-1	379.8	966.4
SWIR-2	355.5	857.5
PAN	191.2	185.0
TIRS-1	604.2	435.5
TIRS-2	593.4	345.2

Table A3. Complete table of Overlap Detector Metric Comparison; red data is statistically the worst, followed by yellow data, and green data is statistically the best; if multiple cells are the same color that data is statistically the same as proven by the t-test.

	Greenland Snow Scenes			Mediterranean Sea Scenes		
Band	CPF (10^{-3})	Periodic Model (10^{-3})	Nearest SS (10^{-3})	CPF (10^{-3})	Periodic Model (10^{-3})	Nearest SS (10^{-3})
C/A	1.81	0.998	1.37	3.69	3.32	3.46
Blue	1.16	1.09	1.02	2.58	3.35	3.48
Green	1.25	0.809	0.817	11.52	11.45	12.52
Red	1.12	0.724	0.937	16.24	16.53	17.78
NIR	0.882	0.845	1.47	23.90	24.22	25.69
SWIR-1	14.43	14.41	7.92	65.86	65.80	59.33
SWIR-2	8.69	7.30	4.17	64.07	62.64	60.76
PAN	1.09	0.610	1.59	3.98	4.22	5.33
TIRS-1	15.03	10.52	16.41	8.07	3.69	15.00
TIRS-2	28.02	14.70	12.78	29.61	5.27	13.11

	Australian Desert Scenes			Arabian Desert Scenes		
Band	CPF (10^{-3})	Periodic Model (10^{-3})	Nearest SS (10^{-3})	CPF (10^{-3})	Periodic Model (10^{-3})	Nearest SS (10^{-3})
C/A	3.09	4.49	3.90	2.78	0.778	1.90
Blue	2.63	3.93	3.81	2.25	0.826	1.47
Green	4.83	5.91	6.33	1.89	0.549	1.89
Red	2.90	3.80	4.81	1.42	0.389	1.73
NIR	2.12	2.84	4.06	1.14	0.325	1.59
SWIR-1	3.11	3.59	4.05	2.02	0.805	7.55
SWIR-2	4.16	3.25	4.20	1.73	0.807	4.08
PAN	1.36	2.22	2.17	1.18	0.323	2.59
TIRS-1	7.29	2.81	16.90	6.51	1.70	18.83
TIRS-2	29.62	3.31	18.22	29.50	2.37	20.72

	Amazon Forest Scenes			Antarctica Snow Scenes		
Band	CPF (10^{-3})	Periodic Model (10^{-3})	Nearest SS (10^{-3})	CPF (10^{-3})	Periodic Model (10^{-3})	Nearest SS (10^{-3})
C/A	8.63	8.59	8.71	1.84	2.69	1.63
Blue	12.47	12.55	12.62	1.79	1.39	1.56
Green	13.58	13.49	14.12	1.19	1.77	1.43
Red	17.28	17.16	17.83	1.15	1.10	1.24
NIR	4.94	4.96	5.80	1.26	0.896	1.16
SWIR-1	33.23	33.26	32.94	4.60	4.02	9.90
SWIR-2	55.20	55.16	55.45	6.49	6.73	9.89
PAN	10.17	9.86	10.24	1.56	0.966	1.09
TIRS-1	9.70	5.35	14.80	20.02	13.43	14.77
TIRS-2	29.45	7.79	15.29	30.30	20.77	9.55

N. African Desert Scenes

Band	CPF (10^{-3})	Periodic Model (10^{-3})	Nearest SS (10^{-3})
C/A	2.38	0.866	1.45
Blue	2.01	0.72	1.08
Green	1.66	0.775	1.34
Red	1.37	0.644	1.19
NIR	0.978	0.430	1.43
SWIR-1	1.80	1.00	7.69
SWIR-2	0.835	1.07	4.41
PAN	1.07	0.513	2.74
TIRS-1	5.99	2.02	18.57
TIRS-2	30.42	2.61	18.28

LITERATURE CITED

1. NASA. The Worldwide Reference System. Available online: https://landsat.gsfc.nasa.gov/about/the-worldwide-reference-system/ (Accessed on 21/01/22).
2. United States Geological Survey. Landsat 7 (L7) Data Users Handbook. Available online: https://prd-wret.s3.us-west-2.amazonaws.com/assets/palladium/production/atoms/files/LSDS-1927_L7_Data_Users_Handbook-v2.pdf (Accessed on 21/01/22).
3. United States Geological Survey. Landsat 8 (L8) Data Users Handbook. Available online: https://d9-wret.s3.us-west-2.amazonaws.com/assets/palladium/production/s3fs-public/atoms/files/LSDS-1574_L8_Data_Users_Handbook-v5.0.pdf (Accessed on 21/01/22).
4. Hillen, F. IGF Studenprojekt. Available online: http://www.florianhillen.de/studium/projekt/index.php?id=grundlagen&uid=sensoren (accessed on 21/01/22).
5. Pesta, F. "Relative Radiometic Characterization and Correction of the Landsat 8 OLI Using the OnOrbit Side-Slither Maneuver" (2015). Electronic Theses and Dissertations. 1773.
6. Knight, E.J.; Kvaran, G. Landsat-8 Operational Land Imager Design, Characterization and Performance. Remote Sens. 2014, 6, 10286-10305. https://doi.org/10.3390/rs61110286
7. Markham, B.; Barsi, J.; Kvaran, G.; Ong, L.; Kaita, E.; Biggar, S.; Czapla-Myers, J.; Mishra, N.; Helder, D. Landsat-8 Operational Land Imager Radiometric

Calibration and Stability. Remote Sens. 2014, 6, 12275-12308. https://doi.org/10.3390/rs61212275

8. Shrestha, A.K. Relative Gain Characterization and Correction for Pushbroom Sensors Based on Lifetime Image Statistics and Wavelet Filtering. Electrical Engineering and Computer Science Department, South Dakota State University, 2010.

9. Wegener, M. Destriping multiple sensor imagery by improved histogram matching. International Journal of Remote Sensing, 11:5, 859-875, DOI: 10.1080/01431169008955060

10. Cook, M.; Peterson, B.; Dial, G.; Gibson, L.; Gerlach, F.; Hutchins, K; Kudola, R.; Bowen, H. "IKONOS technical performance assessment", Proc. SPIE 4381, Algorithms for Multispectral, Hyperspectral, and Ultraspectral Imagery VII, (20 August 2001); https://doi.org/10.1117/12.43699

11. Pesta, F.; Bhatta, S.; Helder, D.; Mishra, N. Radiometric Non-Uniformity Characterization and Correction of Landsat 8 OLI Using Earth Imagery-Based Techniques. Remote Sens. 2015, 7, 430-446. https://doi.org/10.3390/rs70100430

12. United States Geological Survey. Landsat 8-9 Calibration and Validation (Cal/Val) Algorithm Description Document (ADD). Available online: https://d9-wret.s3.us-west-2.amazonaws.com/assets/palladium/production/s3fs-public/atoms/files/LSDS-1747_Landsat8-9_CalVal_ADD-v4.pdf (Accessed on 21/01/22).

13. United States Geological Survey. Landsat 1-9 Calibration Parameter Files (CPF). Available online: https://landsat.usgs.gov/calibration-parameter-files-search (accessed on 21/01/22).

14. United States Geological Survey. Response Linearization Look Up Tables (RLUT). Available online: https://landsat.usgs.gov/rlut (Accessed on 21/01/22).

15. Niveos.cnr.it. 2022. SISpec | Snow \& Ice Spectral Library. [online] Available at: https://niveos.cnr.it/SISpec/ (Accessed on 21/01/22).

16. Shepherd, Keith D., et al. "Rapid characterization of organic resource quality for soil and livestock management in tropical agroecosystems using near-infrared spectroscopy." Agronomy Journal 95.5 (2003): 1314-1322.

17. Bourke, P. "Cross correlation, autocorrelation, 2d pattern identification." (1996). Research Gate 2019.

18. Pearson, R.K.; Neuvo, Y.; Astola, J. et al. Generalized Hampel Filters. EURASIP J. Adv. Signal Process. 2016, 87 (2016). https://doi.org/10.1186/s13634-016-0383-6 (Accessed on 21/01/22).